University of Zurich

Physics institute

ÉCOLE POLYTECHNIQUE FÉDÉRALE DE LAUSANNE

Spring 2012
Master Thesis

Preparations for measurements of the low energy response of liquid xenon

Composer :	Payam Pakarha
Supervisors:	Prof. L. Baudis & Prof. M. Ribordy
Cosupervisor:	Dr. A. Manalaysay

Acknowledgments

During the period of my Master thesis, I have been communicating with many people who supported me kindly while, to only some of whom it is possible to give particular mention here.

First, I would like to mention Hesam, Ehsan, Mehrdad and Iman whom I lived together with among the first year of my studies as a master student in Lausanne. Specially, I'd like to thank Ehsan since he introduced me Latex and tried to recommend me using it. Hesam also for his powerful ability in computer handling who resolved any problem I had with computers.

Thank to Prof. Riccardo Rattazzi and Dr. Simone Andrea who supervised me on my two semester projects (TP(I),(II)) at cole Polytechnique Fdrale de Lausanne. It was very helpful and enjoying working with your group on theoretical particle physics.

To David Heymes, my best friend in first two semesters in Lausanne. I enjoyed studying together for the exams and still remember the last time we met before you leave to Germany. I hope to see you soon again.

I particularly thank Carmelina Genovese first, as our secretary at physics department, university of Zurich since helping me for documentations and paperwork. Second, as a friend who helped me out of her duty to find a flat in Zurich.

Giovanni Benato for hosting me and my wife while we had nowhere to stay in Zurich and helping us to move to our new flat and also it was very nice to have breaks with you while I was working on my project.

Manuel, Kiran and Giovanni who worked with me in the same office. Thanks for your helpful answers to all major and minor questions I asked in the meanwhile.

Dr. Alexander Kish, Annika, Gaudenz, Michael, Francesco, Andreas, Daniel, and Dr. Marc Schumann, my colleagues at L. Baudis group. It is great to be in the same group as you are. I also thank Marc and Alex for their helpful scientific support whenever I needed.

Dr. Teresa Marrodan Undagoitia for her kind and brilliant support since I started my Thesis writing. I found your comments pretty constructive. I was undoubtedly unable to write this without your help.

Dr. Aaron Manalaysay for his wise supervision of my master project. I consider it a luck having the chance of working under the supervision of you. your suggestions and solutions to the problems guided this project into the right path.

Prof. Mathieu Ribordy, my supervisor at EPFL. I really appreciate that you accepted my supervision while neither I was a former student of you and the project

was very completely consistent with your field of interest. I would have not officially been able even to start this project if you had not accepted my request.
Prof. Laura Baudis my supervisor at UZH. First, I am very glad that you accepted me as a master student in your group. Next, It was very nice to work under your supervision together with the powerful group of yours.
Thanks to my parents as well as my parents in law for Supporting me and Saghar both emotionally and financially while suffering being far from your children. I hope I can compensate some of this doing my best to make you proud.
And finally, I thank my lovely wife, Saghar Nabavi, for her patience and her kind support in this while. The fact that I'm living with you has always been my sweetest dream.

Contents

1 Introduction

1.1 Dark Matter, WIMPs and Searches

Studying galactic rotational curves, gravitational microlensing and cluster collisions have provided strong evidences for presence of some non-baryonic source of matter in the universe [1, 2]. Studying the structure formation of the universe requires the dark matter to be cold and long-lived.
While many dark matter candidates have been proposed, with varying degrees of justification, none of the existing observations can tell us much about its identity. Among these candidates, WIMPs (weakly interacting massive particles) are the most promising. WIMP refers to massive particles with $m_{WIMP} \approx 10$ to 10^4 GeV which interact with normal matter only due to weak interactions and the gravity.
The standard model of particle physics can't provide an explanation for presence of WIMPs. This fact motivates theories behind standard model as for example, some theories using supersymmetry (SUSY) propose particles which have the features of WIMPs [5] e.g their mass, relic abundance, and their temperature (coldness) at decoupling.
The nature of dark matter is still unknown. Therefore, experimental physicists investigate ways to build up detectors in which observing dark matter interactions is possible. These experiments are divided into two major types.
First type of experiments aim to detect not the dark matter itself, but products of its decay, annihilation, self-annihilation or co-annihilation. Thus, they are referred to indirect dark matter searches (see for example [3, 4]). In contrast, other type of experiments are probing dark matter's interaction with normal matter. Figure 1 shows the latest results of a number of direct dark matter detection experiments.
Among direct detection DM seraches, XENON100 [6, 7, 8] experiment is connected to this work and is briefly described in the following chapters. This experiment has an exclusion line shown with solid blue in the figure. An exclusion line means that after some while (typically 1 year) of data taking with the experiment which is sensitive to the phase region above the exclusion curve, no possible signal is observed in the experiment. As it is shown in the figure, the new result of XENON100 experiment has the highest sensitivity.
There are more experiments which have their own region of exclusion. For example, ZEPLIN-III [24] and CDMS-II [15]. However, some other experiments have possible signal in certain regions marked with closed curves in this figure. For instance, DAMA [13], COGENT [14], and CRESST-II [16] experiments have proposed their

respective possible signal regions.
The gray colored section is the region of interest of SUSY models. The green and yellow colored sensitivity regions correspond to ±1 and ±2 σ expected limit of the last run (2012) of XENON100 experiment respectively.

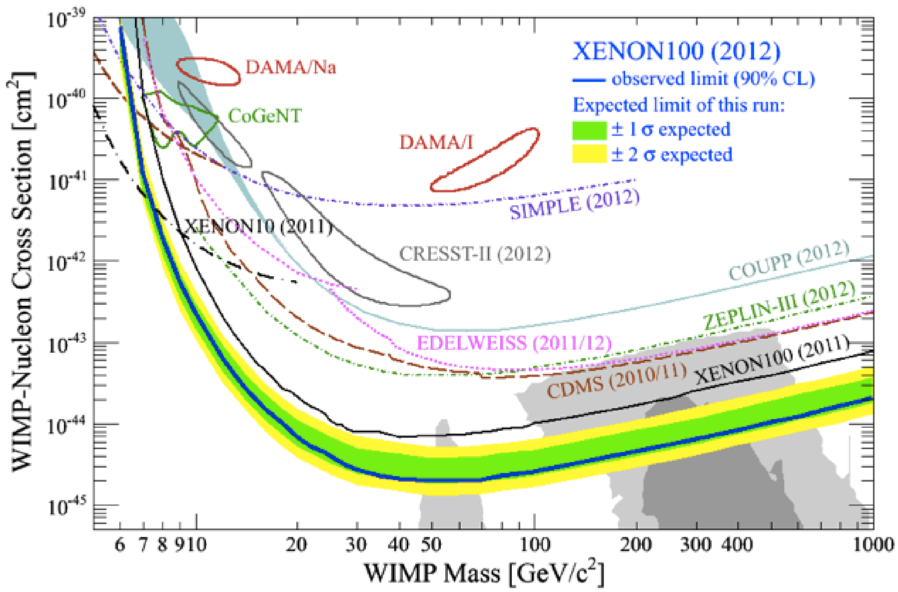

Figure 1: Latest results of direct detection dark matter searches. Figure from reference [17].

1.2 Dark Matter Searches with Liquid Xenon

WIMPs, if they exist, interact with normal matter via an elastic scattering with target nucleus which causes a low-energy nuclear recoil [18]. This is the strategy which pursues a direct detection of dark matter. The first challenge for these studies is that the rate of such interactions, as predicted, would be extremely low. However, after years of scientific and technological progress, physicists able to build detectors sensitive to these rare interactions.
The main background of these processes are gamma rays emitted from radioactive isotopes in the materials of detector. One has to avoid the background rate to dominate over rare signals from WIMP interactions. This fact, raises the level of importance of choosing the proper target material in which distinguishing the background signal from main interaction is more reachable. Besides, proper shielding

of the detectors against active materials should be considered as well as installing detectors underground in order to avoid cosmic ray backgrounds to dominate the signal.

Recently, LXe (liquid xenon) has come into significant interest for dark matter searches [19, 20]. Using LXe, one can take advantage of measuring scintillation and ionization light simultaneously [21]. This is due to the interaction of the incoming particle with xenon atoms which produces ionized and electrically excited xenon atoms. Some of the released ionization electrons might survive electron-ion recombination and drift out of the interaction site to be collected. In addition, excited atoms plus the recombined electron ion pairs will produce 178 nm scintillation photons [22].

LXe has several advantages as target material. First, the cross section for spin independent interaction of WIMP elastic interaction with matter is approximately proportional to A^2 where A is the atomic mass of the target nucleus i.e. $\sigma \propto A^2$ [23]. A comparison between a few differential recoil interaction rate of different target materials is shown in the Fig. 2.

Second, due to its high atomic number (Z), LXe is an efficient gamma absorber (gamma rays are the main background of these detectors as they produce electronic recoils in the target nucleus which yields a scintillation signal). This means that the amount of background interacting with active volume in a liquid xenon detector is reduced by the outer layers of the volume. This effect is called self-shielding. Additionally, there are not many long-lived radioactive xenon isotopes (only ^{136}Xe radiating via double beta decay measured by EXO experiment [26]), which makes LXe preferable with respect to argon for example.

Finally, to scale up a LXe detector mass (for ten times for instance) is respectively easy in contrast to crystal scintillators. This is a big advantage for a dark matter experiment since more active material will increase the signal rate linearly as well as decreasing the background by self-shielding property. Since the exact interaction rate of dark matter in unknown, having the opportunity of scaling up a detector is the strategy of most of dark matter experiments.

The XENON100 experiment is currently one of the most sensitive dark matter search in operation [6]. This experiment uses LXe in a time projection chamber (TPC) to search for xenon nuclear recoils resulting from the scattering of dark matter. The active target of XENON100 contains 62 kg of LXe, surrounded by an LXe veto of 99 kg, both instrumented with photomultiplier tubes (PMTs) operating inside the liquid or in xenon gas. The LXe target and veto are contained in a low-radioactivity stainless steel vessel, embedded in a passive radiation shield and is installed underground at the Laboratori Nazionali del Gran Sasso (LNGS), Italy [8].

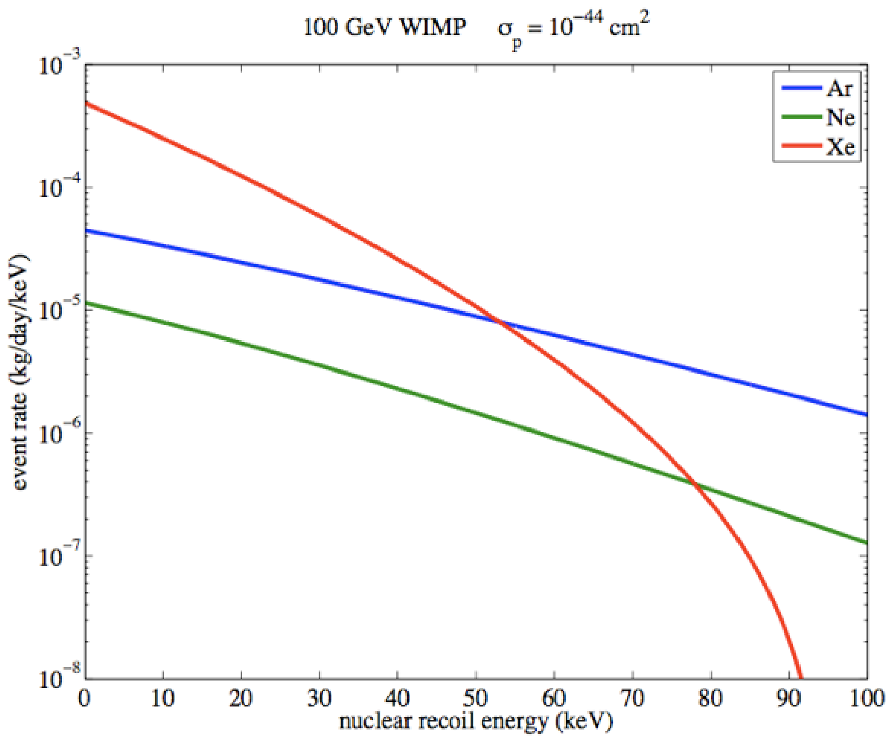

Figure 2: Differential rate of interaction of 100 GeV WIMPs with different noble gas target materials. Figure from Aaron Manalaysay.

The experiment has recently published results from a 225 livedays dark matter search [6] resulting the best limit of a spin-independent WIMP-nucleon scattering cross section sensitivity of $\sigma = 2 \times 10^{-45}\,\mathrm{cm}^2$ for $55\,\mathrm{GeV}/c^2$ WIMP mass.
In this detector, two signals are considered. The S_1 signal, the scintillation light caused by excitation of xenon atoms via interaction with incoming particle, and the S_2 signal is due to the electrons released by ionization of LXe and survived the electron-ion recombination and finally, gathered in the gas phase above the liquid. The ratio of S_2/S_1 signal allows for discrimination of nuclear recoils signal from electron recoils signal caused by incoming gamma rays, and β decays which is the background of these measurements. A schematic view of a xenon TPC together with waveform examples of nuclear and electron recoils are shown in the Fig. 3.

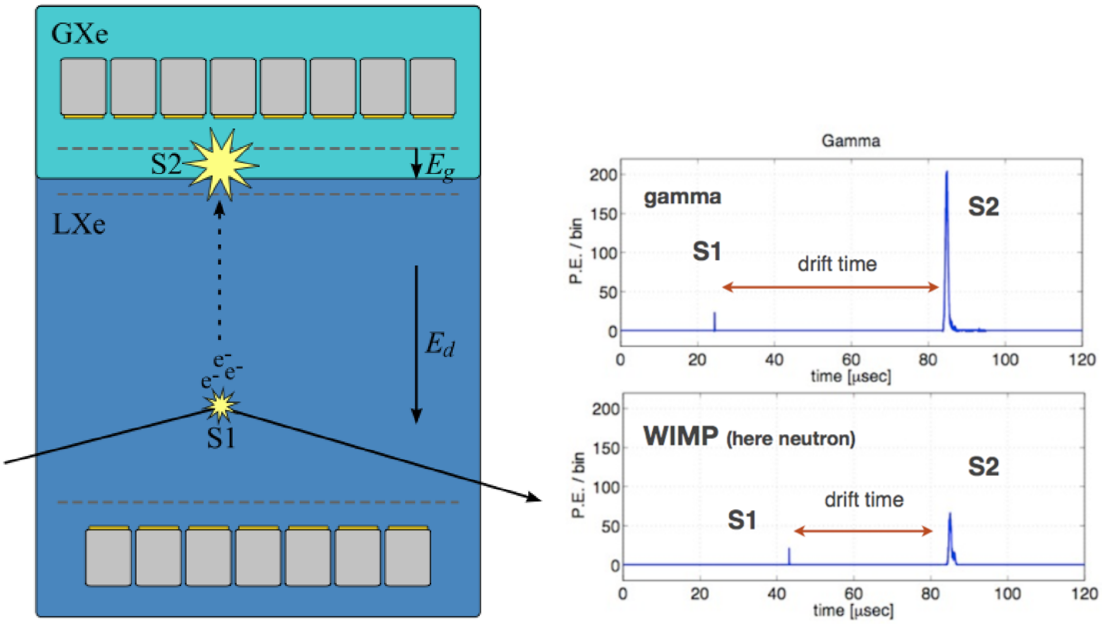

(a) (b)

Figure 3: a) Schematics of the XENON two-phase liquid-gas time projection chamber (TPC). b) Sketch of the waveform of two type of nuclear recoils (down) versus electron recoils (top). Figures from Aaron Manalaysay.

1.3 Response of Liquid Xenon to Low-Energy Nuclear Recoils

One important feature shown in Fig. 2 is that the cross-section is decreasing (almost) exponentially with respect to the recoil energy. It can be seen that if a low-energy threshold is achieved in LXe, a large rate is expected.
In addition, low-energy range of recoils is the least studied among direct dark matter searches i.e though many direct measurements exist in the literature [9, 10, 11, 12, 43, 44, 50] , only few of these provide coverage below $\approx$10 keV [43, 44, 50].
However, in order to produce low-energy recoils in a detector, using WIMPs is not possible as a beam of WIMPs in not in hand. Therefore, neutrons of few MeV are used for this purpose as they will also scatter with target nucleus causing nuclear recoils. Thus, to study low-energy response of LXe (or any other material) to nuclear recoils, one has to provide a monoenergetic beam of neutrons.

In chapter 3, it is described in detail how we take advantage of a neutron beam to study low-energy recoils in a liquid scintillator target. Monoenergetic recoil energy is achieved via selecting neutrons of a fixed scattering angle. Finally, an experiment is setup at University of Zürich in which S_1 and S_2 signals can be measured directly in a TPC.

1.4 Measurements of $\mathcal{L}_{eff}$ and Q_y

Studying S_1 and S_2 signals in LXe, has shown that the ionization and scintillation energies do not represent a linear behavior with respect to number of detected electrons and photons. In fact, some quenching behaviors are observed. In addition to exciting and ionizing the target atoms, an interacting particle in the active volume, might loose energy due to other processes which, if ignored, will cause an understimation of the deposited energy.
In the case of the scintillation response of LXe to WIMPs, three processes may affect the energy deposition procedure as the following:

- Lindhard Quenching: If the projectile and the target material are in the same range of masses, the energy might transfer from projectile particle to target particles via elastic collisions adding heat to the target material without any detectable emission. This pursues underestimating the energy of projectile [27].

- Bi-excitonic quenching: In the situation where the density of excitons (excited atoms) is high, the following process might happen before the particle's deexcitation [28]

$$\mathrm{Xe}^* + \mathrm{Xe}^* \longrightarrow \mathrm{Xe}^+ + \mathrm{Xe} + \mathrm{e}^-. \tag{1}$$

- Electron-Ion recombination: An escaping electron recombines with a Xe_2^+ ion and lefts a double exited xenon atom [29] via the following interactions

$$\mathrm{Xe}^+ + \mathrm{Xe} \longrightarrow \mathrm{Xe}_2^+ \tag{2}$$
$$\mathrm{Xe}_2^+ + \mathrm{e}^- \longrightarrow \mathrm{Xe}^{**} + \mathrm{Xe} \tag{3}$$
$$\mathrm{Xe}^{**} \longrightarrow \mathrm{Xe}^* + \mathrm{heat}. \tag{4}$$

The parameter, "scintillation yield"is defined as the number of scintillation photons produced per unit energy. This parameter is dependent on the type of incoming

particle as well as its energy [27, 28]. The relative scintillation efficiency of nuclear recoils ($\mathcal{L}_{eff}$) is used to quantify the quenching. This quantity converts the scintillation signals of dark matter interaction in LXe into recoil energies [44].
It is difficult to predict the light yield in absolute terms as it depends on a number of factors, including the energy and identity of the particle. Therefore, $\mathcal{L}_{eff}$ is defined as the light yield of nuclear recoils relative to that of 122 keV gamma rays from ^{57}Co. As mentioned above, the light yield depends on the electronic stopping power ($\frac{dE}{dx}$), which depends on the energy of the particle, and therefore $\mathcal{L}_{eff}$ is an energy dependent quantity [51].
The same argumentation, as we discussed about the scintillation, is true about the ionization yield. Parameter Q_y is defined as absolute ionization yield of LXe. Different groups studying dark matter detection in LXe, have made efforts to measure this parameter in the interesting range of recoil energy (for example, see [12]).
The uncertainty in the nuclear recoil energy scale at low energies is the largest systematic uncertainty in the reported results from LXe WIMP searches [6, 7, 8, 24, 25]. In order to decrease the uncertainties of this parameter, many groups are running experiments [44, 32, 50, 51, 52] and the latest results are shown in Fig. 4.
The solid line in this figure shown the best fit to the results. Results of different experiments are marked in different colors. The blue bands correspond to 1σ and 2σ of uncertainty. The aim of these studies is to decrease the error bars shown in this figure and to measure $\mathcal{L}_{eff}$ down to the lowest possible energies.

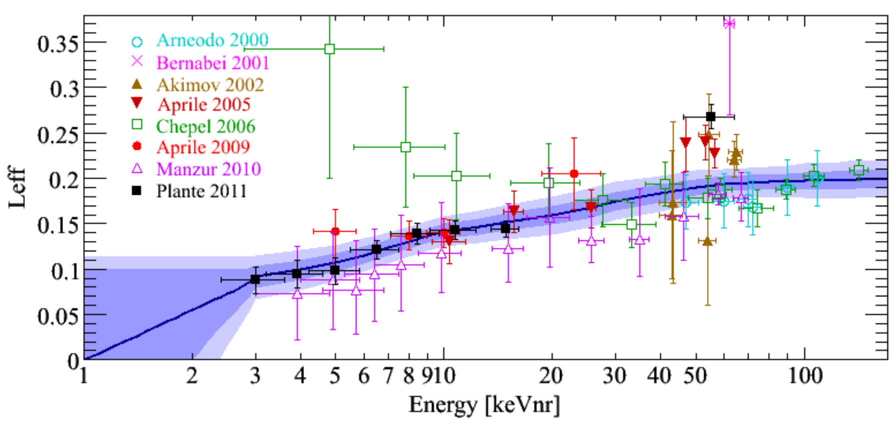

Figure 4: Recent measured values of $\mathcal{L}_{eff}$ versus recoil energy. The aim of $\mathcal{L}_{eff}$ measurements is to decrease the uncertainties which causes the errorbars become smaller as well as moving toward lower recoil energies. Figure from reference [17].

A small LXe prototype detector has been constructed at the University of Zürich in order to test liquid xenon response to low-energy ionizing radiation, called the Xürich detector [48]. The schematics of the detector are shown in Fig. 5. For detailed technical information about the detector's design and performance see reference [48].

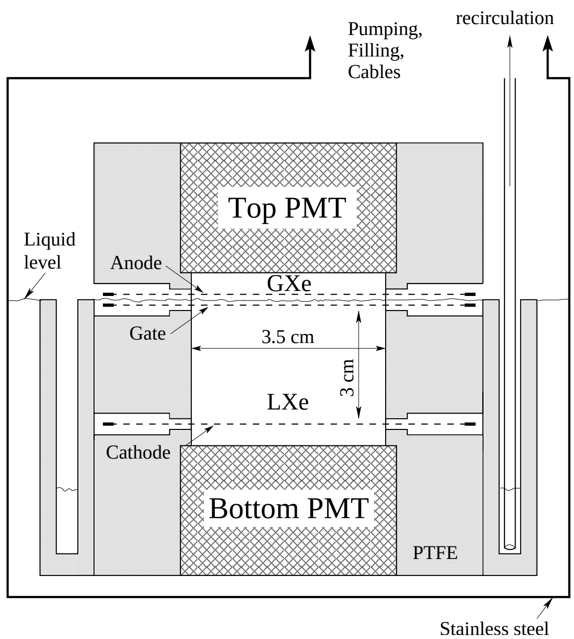

Figure 5: Schematic view of *Xürich* detector. Figure from reference [30].

It is decided to use this detector (actually, a modified version of Xürich detector) for $\mathcal{L}_{eff}$ and Q_y measurements. This requires placing the detector in front of a neutron beam and observe the neutrons with a detector after their scattering with liquid xenon target. The principles of the experimental setup as well as the physics of these studies are discussed in section 3.2.
The focus point of this work is to perform preparations for these measurements. This includes characterizing the basic components which will be used in the final setup such as the neutron generator,pulse shape discriminator module and detectors. In the following chapters this works are described in detail.

2 Pulse shape discrimination with Organic Liquid Scintillators

2.1 Motivation

The aim of this chapter is to study the response of a liquid organic scintillator detector to interacting particles and characterize their ability to distinguish a nuclear recoil (neutrons) from electronic recoils (gammas).
This characterization is very important as two of these scintillators are to be used for the experiment which is described in chapter 3. The gammas, producing electronic recoil signals in scintillator, are the background of these studies and discriminating background from the main signal caused by neutrons is vital.
EJ301 is the name of the liquid scintillator we use for our measurements and it contains $C_6H_4(CH_3)_2$ as the active scintillation material, which is also known by the proprietary names BC501A and NE213 [34] (see Fig. 8).
The target scintillator atom which is hit by an incoming particle might excite into triplet or singlet states. If it is excited into a singlet state, it will de-excite emitting a fluorescence scintillation light. However, it also often happens that due to bimolecular interactions, the triplet state being converted to a short-lived singlet state resulting a delayed fluorescence signal. These reactions are explained in detail in references [33, 45, 49].
The rate of these bimolecular interactions depends on the density of triplet states, which in turn depends on the rate of energy loss $\frac{dE}{dx}$ of the recoiling particle. Thus, the tails of pulses resulting from nuclear recoils (high $\frac{dE}{dx}$) will be characteristically longer than those from electronic recoils (low $\frac{dE}{dx}$)[33].
This fact motivates to study the pulse shape as a discrimination parameter. For example, the response of a liquid scintillator is plotted for a gamma particle together with the response to neutrons with three different energies (see Fig. 6). The difference in the shape of the tail of the pulses corresponding to nuclear and electron recoils is used to distinguish them.

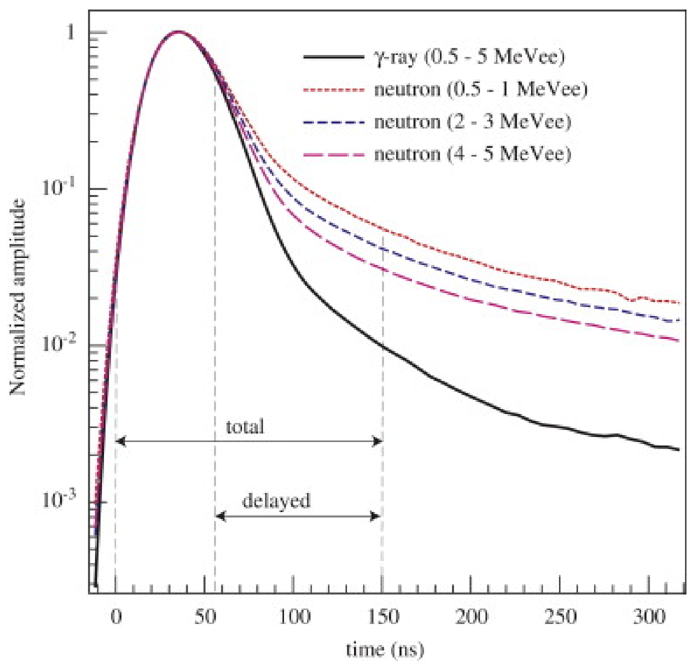

Figure 6: Response of an example liquid scintillator to a gamma particle and a neutron particle with three different range of energies. The pulses are normalized for comparison. Figure from reference [37].

2.2 Experimental Setup

The schematic setup for pulse shape analysis is shown in the Fig. 7. A detector (EJ301) is placed in front of a radioactive source. The photomultiplier tube (PMT) that is detecting scintillation from EJ301 is powered by a high-voltage module (HV=-1400 V) and the signal goes to electronic readout. Each part is shortly described in the following.

2.2.1 Sources

As mentioned in section 1.4, neutrons are used to produce nuclear recoils in the target. Gamma rays are the background of these studies. However, they are also often used for calibration of the recoil energy.
Thus, we need sources providing gammas and neutrons. There is no radioactive

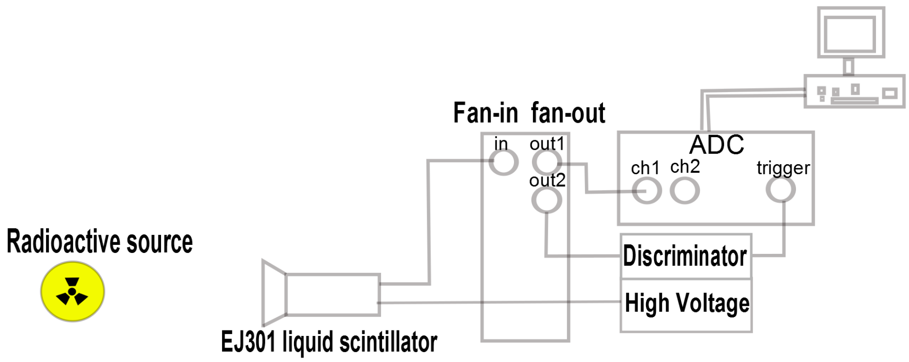

Figure 7: Schematics of the experimental setup for pulse shape discrimination studies.

source which produce only neutrons (no gammas). However, there are sources radiating neutrons and gammas simultaneously. ^{241}AmBe source is used as a the neutron source in this work. As gamma sources, ^{22}Na and ^{57}Co are used (^{137}Cs is used also for calibration). The interactions describing activities of the sources are described individually below:

^{241}AmBe : Americium emits an alpha particle first which might be absorbed by the beryllium and emits neutrons plus the stable carbon. The half life of the alpha emission is 432 years. Each of these two interactions emit an additional gamma [35]. This process is called (α,n) reaction. The resulting neutrons are used for production of nuclear recoils.

$$ {}^{241}_{95}\mathrm{Am} \longrightarrow {}^{237}_{93}\mathrm{Np} + {}^{4}_{2}\alpha + \gamma \tag{5} $$

$$ {}^{4}_{2}\alpha + {}^{4}_{9}\mathrm{Be} \longrightarrow \mathrm{n} + {}^{6}_{12}\mathrm{C} + \gamma \tag{6} $$

^{22}Na : This isotope emits gamma rays at 511 and 1275 keV [36]. The half life of this isotope is 2.6 years. The 1.275 MeV gamma follows to the β_+ emission which leaves the nucleus in an excited state at this energy and the 511 keV gamma is due to the electron positron annihilation.

$$ {}^{22}\mathrm{Na} \longrightarrow {}^{22}\mathrm{Ne}^{*}\,(1\ \cdot 275\ \mathrm{MeV}) + \mathrm{e}^{+} + \nu \tag{7} $$

$$ {}^{22}\mathrm{Ne}^{*} \longrightarrow {}^{22}\mathrm{Ne}_{\mathrm{g.s}} + \gamma \tag{8} $$

$$ \mathrm{e}^{+} + \mathrm{e}^{-} \longrightarrow 2\,\gamma \tag{9} $$

^{57}Co : This isotope decays into excited ^{57}Fe state by electron capture which then de-excites by emitting a 122 keV gamma ray (85 %) or 136 keV gamma ray (11 %) to the ground state [38]. The half life of the isotope is 271.79 days [39].

^{137}Cs : Through the following reaction, this isotope will produce an excited state ^{137}Ba via β emission. The half life of ^{137}Cs is around 30 years. The excited atom then relaxes to ground state emitting a 662 keV gamma.

$$^{137}\text{Cs} \longrightarrow {}^{137}\text{Ba}^* \,(662 \text{ keV}) + \text{e}^- \tag{10}$$

$$^{137}\text{Ba}^* \longrightarrow {}^{137}\text{Ba} + \gamma \tag{11}$$

2.2.2 Liquid Scintillator Detector

For these measurement an EJ301 detector is used which is built particularly for fast neutron detection and excels for pulse shape discrimination purposes [40]. More technical details exists in the product's data sheet [40]. The schematics of the detector is shown in Fig. 8.

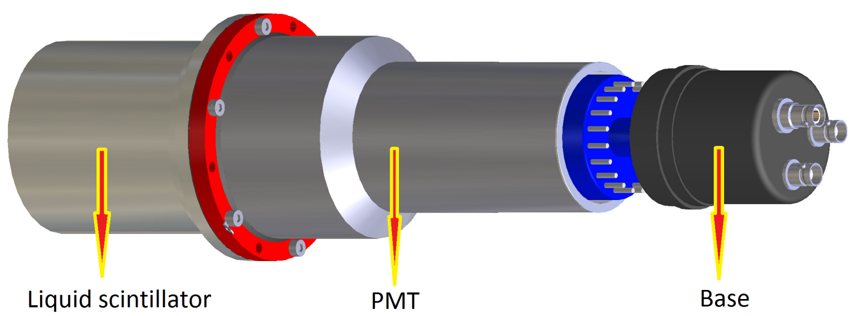

Figure 8: Schematics of EJ301 Liquid Scintillator. The active volume is kept inside metallic holder (left). The container is connected mechanically to a PMT and then an electronic base (right) for signal readout and powering the PMT.

This detector contains a volume of liquid scintillator active material $C_6H_4(CH_3)_2$ which is called commercially as NE213, BC-501A, and EJ301 and is covered by the stainless steel (left) connected mechanically and optically to a PMT which is read by the electronics (right). The high voltage of -1400 V is used to power the detectors.

2.2.3 Readout

The signal cable from the PMT connects the anode of the detector to a fan-in, fan-out module's input, where the signal is split into two outputs, one of which goes to the trigger system while the other is connected directly to an Analog to Digital Converter (ADC) channel. The ADC device is then connected to a PC which controls data acquisition via a Labview [41] program.
The ADC we are using is the made by the company Acquiris (Agilent Technologies) [31]. The discriminator module is set so that it accepts all the signals above a certain threshold.
The computer communicates with the ADCs via Compact PCI (cPCI) connection. The ADC is used at maximum sampling frequency of 1 GS/s.
The second output from fan-out goes into a discriminator module which is used for triggering. The trigger signal then goes into the trigger input of the ADC.

2.2.4 Data Manipulation

Data is stored and then processed to ROOT files. Each event corresponds to a 500 ns waveform. The C++ based ROOT analysis tool [42] is used in order to manipulate the data. Since the anode signal is read, the corresponding voltage is negative and has to be reversed initially to positive. A delay is applied in the Labview program such that the events are saved so that there is $\sim$150 ns of baseline before and after the main pulse. For example, one waveform is shown in the figure **??**.

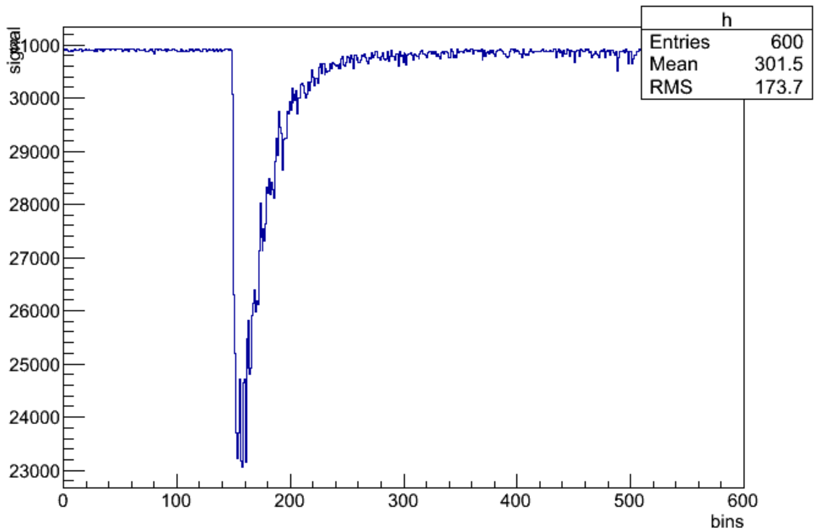

Figure 9: An example of a non-processed waveform.

Numerical average of the first 100 ns (no pulse yet) is used to shift the waveform baseline to 0. The integral of the waveform afterwards is used then to estimate the energy deposited by the particle in the target material. A 4 point calibration is applied to calibrate the energy of electronic recoils. This includes 511 keV, 1275 keV peaks of ^{22}Na and 662 keV of ^{137}Cs and 122 keV peak of ^{57}Co sources. The calibration plot is shown in Fig. 10.

Each source shows a particular spectrum. Full absorption of gammas at these ranges of energies (except probably 122 keV gamma from ^{57}Co) is so unlikely that the Compton scattering interactions will dominate statistically. This is why the Compton edge (caused by back-scattered photons) is seen in the we see in the ^{137}Cs spectrum (Fig. 11) and not the full absorption peak. Equation 12 shows how the Compton edge energy is calculated.

$$E_{edge} = \frac{2E^2}{m_e c^2 + 2E} \tag{12}$$

Where E is the photon energy, m_e is electron's mass and c is the speed of light in vacuum. For example, the fitted spectrum of In this work, the peaks are fitted with a Gaussian function in order to find the mean values. The results of the fits are

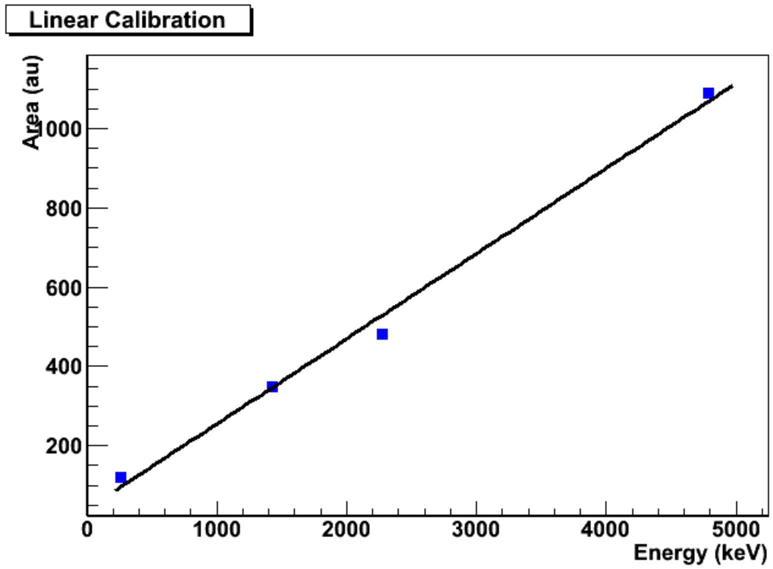

Figure 10: 4 point calibration of electron recoil energies vs signal area. 511 keV, 1275 keV peaks of ^{22}Na and 611 keV of ^{137}Cs plus 122 keV peak of ^{57}Co sources are represented. The red line represents a linear fit to the data points. Errors show how far are the points from the linear fit.

finally used for calibration. For example the fitted spectrum of ^{137}Cs is shown in Fig. 11.

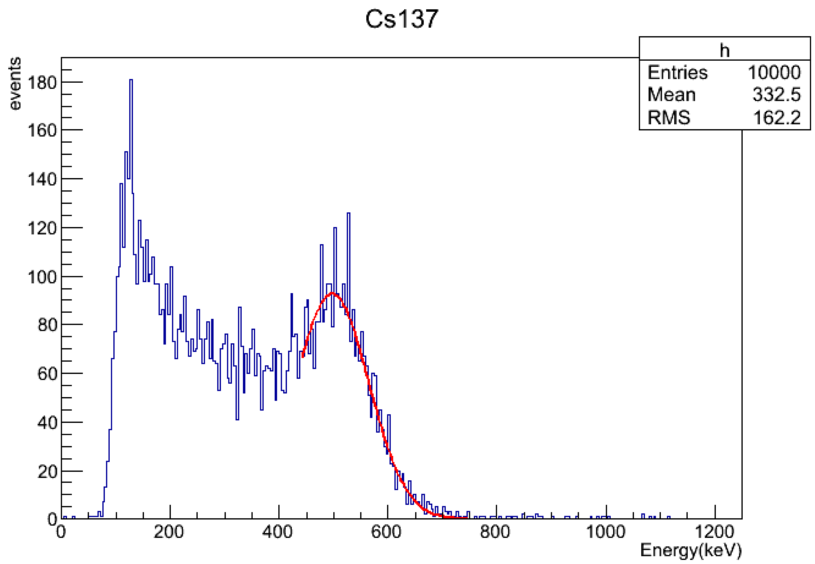

Figure 11: Spectrum of ^{137}Cs radioactive source detected by EJ301 liquid scintillator detector. The Compton edge of the spectrum if fitted with a Gaussian function.

2.3 Data Analysis and Results

As explained in chapter 1, different particles will produce different pulses in liquid scintillators. These differences are used for particle discrimination. This process is called pulse shape discrimination (PSD). Various parameters are used by different groups for discrimination. For example, in reference [44], the height of the signal peak divided by the total area of the signal is used, while in [48] and [32] the tail area of the signal (defined from 30 ns after the peak up to the point where the signal value is as high as 1 % of the peak divided by the total area) is used.
A proper tail definition needs to be defined as well as a parameter to quantify the discrimination quality. As a parameter for quantification, the source acceptance (including gammas and neutrons) of ^{241}AmBe data at the point in which 90 % of gammas from ^{22}Na data are rejected is used. In figure 13 data from both sources is plotted for a PSD parameter and the 90 % rejection line is marked.
In figure 12 the distribution of PSD parameter for various definitions of the pulse tail is shown. One has to compare the source acceptance for each tail definition. The tail definition varies by changing the start and end point of the tail. In particular, the tail starts 10−40 ns and ends at 70−150 ns after the pulse peak. In this figure, four

different tail definitions are applied regarding the start and end points to vary. Blue dots represent data taken ^{241}AmBe (including neutrons and gammas) and red dots represent data taken with ^{22}Na source (only gammas). The PSD value for gammas is lower than neutrons (see section 2.1). The more the neutron and gamma bands are separated, the better the PSD parameter is. Unless the discrimination is the worst at low-energy regions, neglecting low-energy events is not correct since this is the region of the most interest.

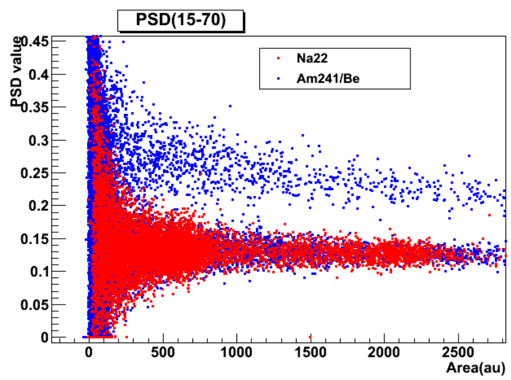

(a) tail is defined between 15 ns and 70 ns after the peak

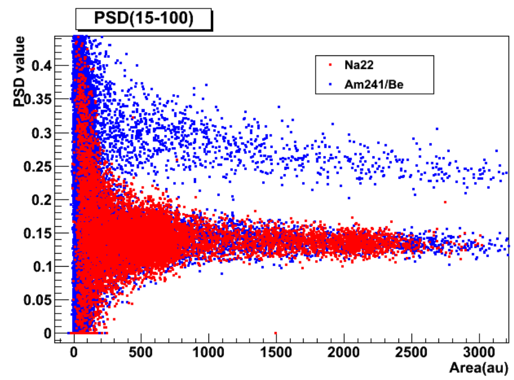

(b) tail is defined between 15 ns and 100 ns after the peak

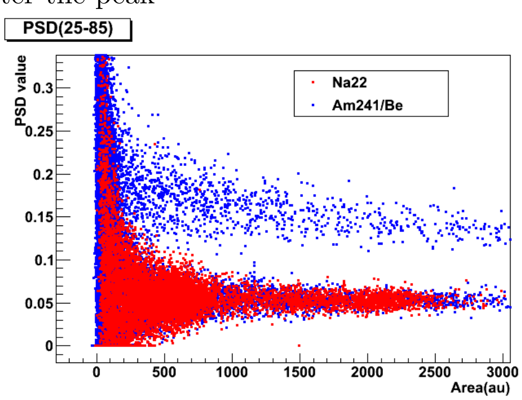

(c) tail is defined between 25 ns and 85 ns after the peak

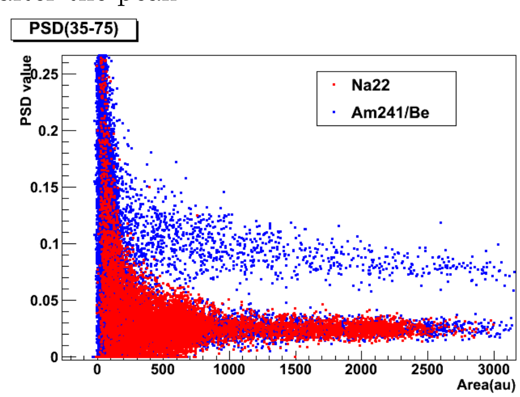

(d) tail is defined between 35 ns and 75 ns after the peak

Figure 12: PSD value versus area of events of a ^{241}AmBe sample (blue) and ^{22}Na sample (red). The more the neutron and gamma bands are separated, the better the PSD parameter is.

The source acceptance at 90 % rejection is achieved considering the plots of PSD parameter populations for ^{22}Na and ^{241}AmBe samples individually. The main peak at both curves represent gammas which covers all of the events from ^{22}Na source and majority of ^{241}AmBe data. Neutrons from ^{241}AmBe source produce either a proton recoil or a carbon recoil in the target. These recoils are populated around PSD values of ≈ 0.15.

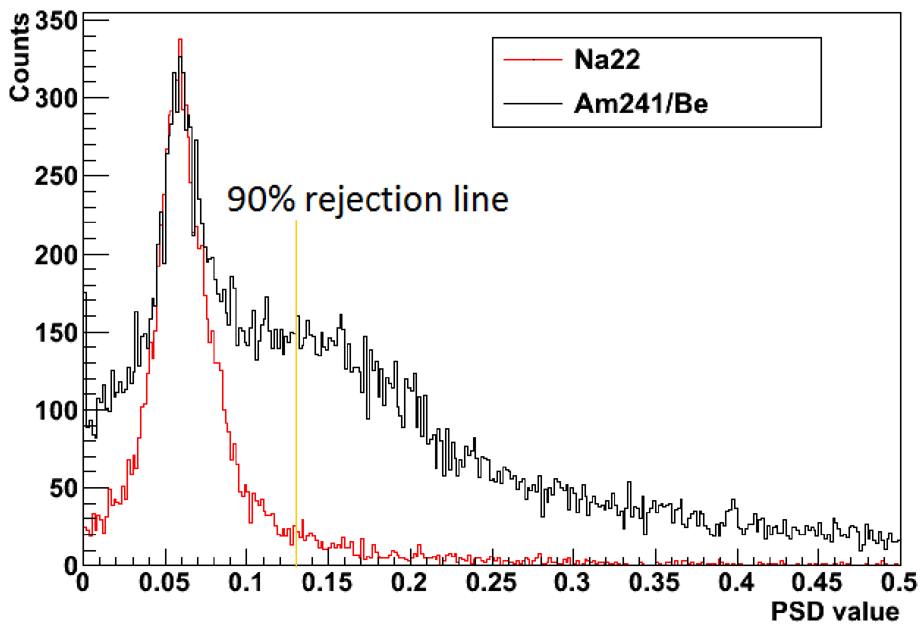

Figure 13: PSD parameter for data taken from ^{241}AmBe and ^{22}Na sources.

As described above, the idea is to quantify the PSD parameter using the acceptance of neutrons at a certain rejection level. This is performed integrating the counts in the gamma sample up to 90 % of the total integral and finding the corresponding PSD value. Thus, the integral of the ^{241}AmBe spectrum above the 90 % rejection line, divided by the total integral corresponds to the source acceptance. The optimal tail definition is the value for which the acceptance is maximized.
Table 1 shows the source acceptance for various tail definitions. These numbers are also represented in Fig 14.

		Starting point of the tail						
		75 ns	85 ns	95 ns	105 ns	115 ns	125 ns	135 ns
End point of the tail	15 ns	31.6 %	32.9 %	34.6 %	36.1 %	37.1 %	37.2 %	37.2 %
	25 ns	33.9 %	35.2 %	37.0 %	38.6 %	39.0 %	39.6 %	39.7 %
	35 ns	34.6 %	36.1 %	38.5 %	39.2 %	39.9 %	40.3 %	40.3 %

Table 1: Source acceptance at 90 % rejection of gammas regarding different tail definitions (different PSD parameter). The numbers in the table are reported in percent. The numbers in the table are reported as percentage of the source acceptance of all events.

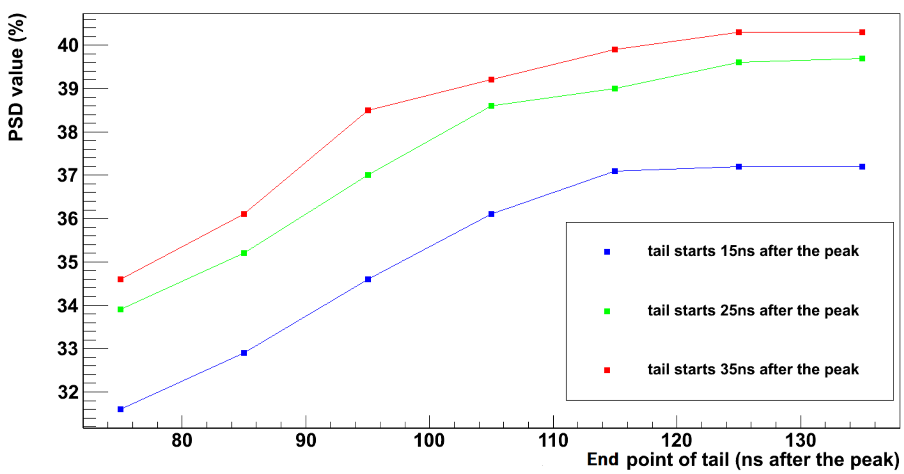

Figure 14: Source acceptance at 90 % rejection of gammas versus the tail definitions. Each curve is drawn for a fixed start point of the tail and the x axis represents the end points in ns after the pulse peak.

The tail is the part of pulse which varies from nuclear to electronic recoils . Thus, the farther we go from the peak to start (and end) our tail the better PSD value (more acceptance) is gained.
However, starting the tail after 35 ns after the peak, though one might expect to see improved source acceptance, does not actually do so. This is because defining our tail after 50 ns for example, causes neglecting all low-energy events whose tails might have been finished already (see Fig. 12). This means that many low-energy nuclear recoils are neglected as well as electron recoils. As mentioned in section 2.3, the

main region of interest in these studies is the low-energy fraction of nuclear recoils (around 3-10 keV) and therefore, these events should not be neglected.

2.4 Characterizing a Pulse-shape Discriminator Module

As mentioned above, it is needed for the study to be able to discriminate gamma particles from neutrons in the setup. Although it is possible to be done reading and processing the raw data (waveform), there are modules designed and optimized for this task.
One of the main modules that has been used in the setup for the neutron measurements is a 4 channel pulse shape discrimination module called MPD-4 from Mesytec company [46].
Each channel has a signal input to read the waveform from PMT and several outputs. Three outputs which are used in our setup are described below[47]:

Ampl: Integrated PMT charge output. The amplitude of this signal is proportional to the area of the input pulse.

TAC: TAC output is used to discriminate nuclear from electron recoils via their fast to slow component ratios. Basically, it is a PSD parameter similar to tail/total ratio that we defined in previous section. The physical content of this parameter is not mentioned in the product's data sheet.

n/γ-Trig: This output can be selected to accept or reject gammas (γ) or neutrons (n), both or neither each of them. In our setup, n/γ trigger output of two channels are used to trigger on coincidence neutrons using a logical module to select the logical "and"of both triggers. This means that the particles are selected if both scintillators detect a particle coincidentally and accept it. Normally, the particle selection is performed in software and the triggers are set to accept all events.

The module has a number of user-adjustable parameters that control performance of its n/γ discrimination ability. In this setup, whenever needed, the device is connected via a USB to the computer and a terminal is used to change the parameters to the desired values.
The other two parameters of interest are called "n-dis"and "walk"and are the subject of this section to be characterized. The basic descriptions of these parameters are the following.

n-dis: hardware discrimination threshold of the TAC output. If the TAC output is below the threshold, gammas are identified, above the threshold neutrons are identified.

Walk: One can take a spectrum "Ampl vs. TAC" with gammas on the scintillator and adjust the curve with the "walk" parameter to get a flat top for the gamma line. This parameter influences the TAC amplitude in the low energy region.

One can thus use a component ratio defined by the integral of the tail of the signals divided by the total pulse integral to discriminate electron/nuclear recoils. We first use a manually defined PSD parameter to check the selection ability of the device and then, start reading the TAC and Ampl outputs of the device.
We use the result of section 2.3 to define the optimized PSD parameter using the best tail definition. Different values of n-dis are tested considering the rejected and accepted events in the PSD vs area plots. Some examples of this work are shown in Fig. 15.
In this figure, all of the events are shown by blue dots. The trigger signal is a step function which appears only when the event is accepted. This leads to select accepted events which are represented as red dots. The higher n-dis parameter is set, more events are accepted as nuclear recoils such that for example in figure (d) a large number of electronic recoils are also accepted in the low energy region. Since the PSD parameter which is defined in this plot is not exactly the same as TAC parameter proposed by the module, the acceptance/rejection border is not very clear. This is indeed the case in figure 16 where the TAC value versus the amplitude of the events is plotted. In this plot, n-dis or equivalently the acceptance/rejection border is clearly a horizontal line.

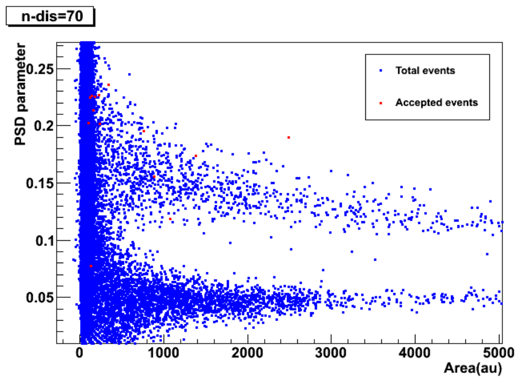

(a) Ndis=70

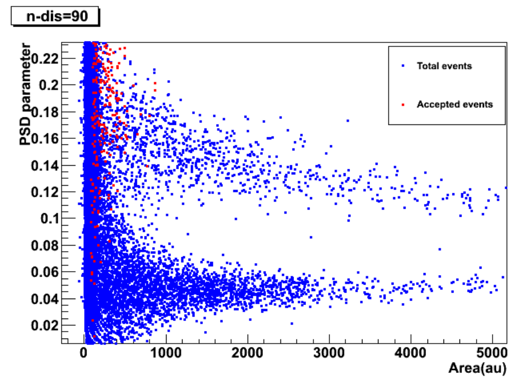

(b) Ndis=90

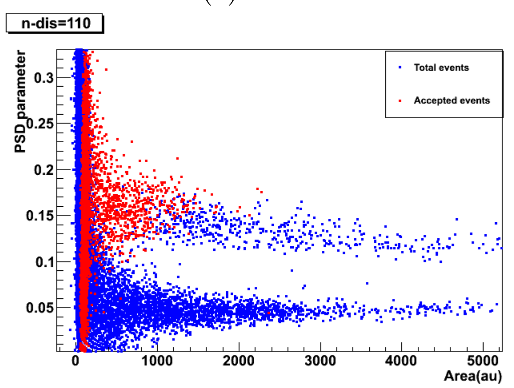

(c) Ndis=110

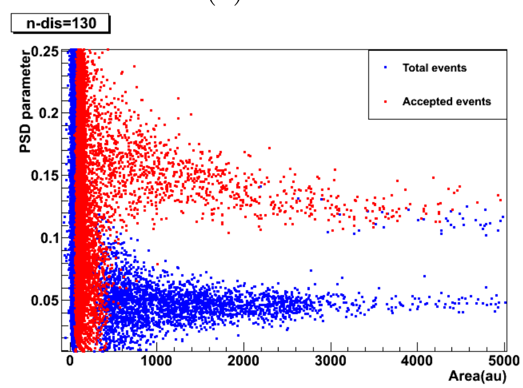

(d) Ndis=130

Figure 15: PSD parameter vs energy (area) of the events.

Instead of using the direct PMT waveform to construct the pulse area and PSD parameter, the Ampl and TAC outputs of MPD-4 module can be used. In the following plots (figure 16) TAC versus Ampl of events is shown, when the n-dis parameter is fixed at 135 and several measurements changing the walk parameter in 5 unit steps are made. Since gammas are considered as background events in the final setup, the optimization of walk parameter is achieved when the gamma band is most straight. The full range of walk parameter is $50-150$ and the default value is 100. Looking at the plots we conclude that a walk value of ≈ 70 are optimal (see figure 16).

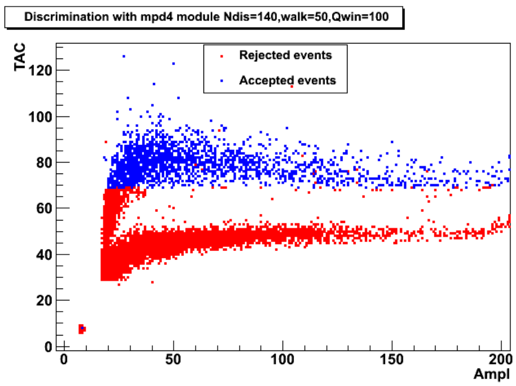

(a) walk=50

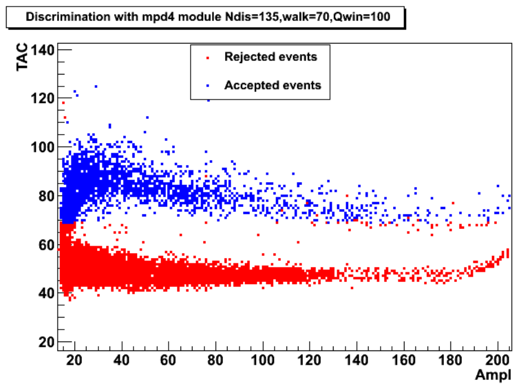

(b) walk=70

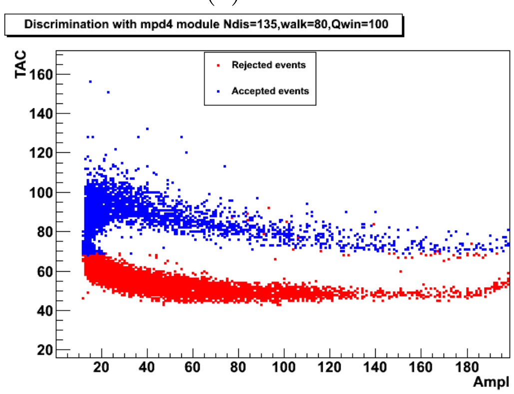

(c) walk=80

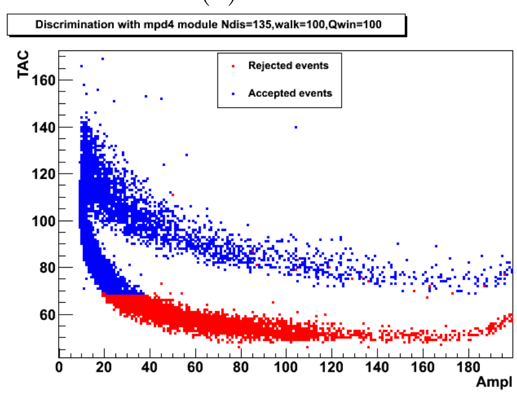

(d) walk=100

Figure 16: TAC vs Ampl of events read by MPD-4

3 Characterization of the Neutron Beam

3.1 Motivation

In this section, we describe a measurement aiming to characterize the neutron beam of a neutron generator. The work contains the setup for the measurement as well as preliminary results of characterization.
The idea is to use Xürich detector described in chapter 1 in order to study the LXe response to the low-energy recoils. The presence of a mono-energetic neutron beam is required to produce nuclear recoils in LXe. This chapter focuses on characterization of the neutron beam.

3.2 Theory

In the setup for this measurement, we use one of the liquid scintillator detectors described in section 2.2.2 in front of the neutron beam and gather the scattered neutrons in a certain angle with another detector to study their features. The complete setup is explained in the next section.
When neutrons (or gammas from background) hit the liquid scintillator material, they will scatter resulting either nuclear or electronic recoils in the atoms of the target. This recoil energy which is deposited in the target is calculated for a nuclear recoil using the kinematics of the scattering interaction. For heavy target atoms (like LXe) which is the case in most of the dark matter detectors, this energy is approximated to be [50, 51, 52]:

$$E_r \approx 2E_n \frac{M_N m_n}{(M_N + m_n)^2}(1 - \cos\theta) \tag{13}$$

where E_r is the energy of the recoiling nucleus, E_n is the energy of the incoming neutron, θ is the scattering angle with respect to the propagation line of the beam, and m_n and M_N represent masses of the neutron and nucleus, respectively. This approximation is valid while the neutron is not relativistic and $M_N \gg m_n$.
Target atoms present in the liquid scintillators which are used for neutron beam characterization are either carbon or hydrogen(see section 2.2.2) . These atoms (hydrogen atoms in advance) don't fulfill the approximation validation condition

$M_N \gg m_n$. Therefore, the exact formula needs to be used [48]:

$$E_r = \frac{2E_n}{(1+A)^2}[1 + A - \cos^2\theta - cos\theta\sqrt{A^2 + \cos^2\theta - 1}] \tag{14}$$

where the notation A is the atomic mass of the target particle species i.e.

$$A = \frac{M_N}{m_n}. \tag{15}$$

A fraction of the neutrons, which scatter from the first liquid scintillator target will hit the second detector which is placed at a certain angle far from the first scintillator. These events are called "coincidences" in this text as the triggers respective to first and the second scintillator are very close to each other in timing ($\Delta t \approx 50\,\text{ns}$). Then, the time difference between the two triggers of a coincidence events correspond to the time in which the particles travel the distance between two scintillators i.e. time of flight (TOF) of particles.
Because the neutron generator is supposed to emit neutrons with the energy spectrum peaked around 2.4 MeV, the neutrons traveling this distance are not relativistic. If we assume for example that the neutron has reached the energy of ~2 MeV after the first scattering, the speed of the neutrons is derived to be ($m_n \approx 1\,\text{GeV}$):

$$E_f = \frac{1}{2}m_n\left(\frac{v}{c}\right)^2 \Rightarrow v \approx \sqrt{\frac{4\times10^6}{10^9}}c \approx 2\times10^7\text{m/s}. \tag{16}$$

This means that by fixing the distance between two detectors at ~2 m, we would expect to see a time of flight spectrum peaked at $t \approx \frac{2}{2\times10^7} = 100\,\text{ns}$. E_f refers to the energy of neutrons after the scattering and according to conservation of energy:

$$E_f = E_n - E_r. \tag{17}$$

Since we know the scattering angle and E_f is computed by TOF, one can simply solve equations 17 and 14 to derive E_n and E_r.

3.3 Experimental Setup

The schematic drawing of experimental setup for the neutron measurements is shown in Fig. 17. A neutron generator is used as the source of neutrons. Two EJ301 liquid scintillators are used for detecting neutrons. In this setup, we use EJ301 both as

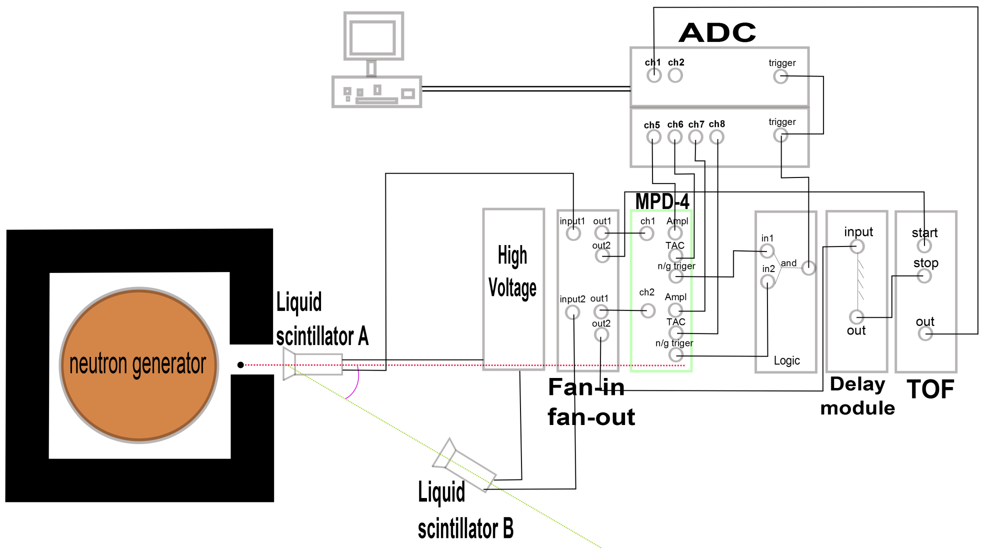

Figure 17: Schematic drawing of setup for neutron measurements with two EJ301 detectors and the neutron generator. Please read the text for complete description.

the target material and detector. The first detector (EJ301A) is used in front of the neutron beam as the active target material and the second (EJ301B) to detect the scattered particles. The detectors are fixed at position mechanically while the distance between the detectors is measured as well as the angle (θ) of the second detectors with respect to the beam's propagation axis.
A measurement of time of flight provides information about the energy of the particles. The MPD-4 module is described in detail in chapter 2.4. The TAC and Ampl outputs of MPD-4 are used to gather data about the type and deposited energy of the particles respectively.
The logical "and" condition of both n/γ trigger outputs of MPD-4 is used as the trigger for a coincidence event meaning a particle who hits the first detector and then the second in less than $\sim$500 ns.
Since we need to digitize 5 different signals two ADC modules are used in parallel (the 1 GS/s ADC can digitize up to 4 inputs). Both ADCs are from company Acquiris. The four channel 1 GS/s ADC is used to digitize two Ampl and two TAC signals from two MPD-4 channels connected to each detector and the 100 MS/s ADC is used to digitize the time of flight signal coming from the time of flight module. Both ADCs share the same trigger as explained.

The signal cable of both detectors go into a fan-in fan-out module and then split to two output signals. One of the outputs of both signals goes into the MPD-4 module. One output signal 2 of the EJ301A goes directly to the "start" of TOF module while signal of the EJ301B goes into a delay module fixed at a certain delay to avoid coincidence inputs and then goes into the "stop" of TOF.
The ADC is then connected to a PC and the same Labview program is used to control the parameters and data manipulation as described in chapter 2.

3.3.1 Detectors

Two EJ301 detectors are used in this setup. These detectors are described in detail in section 2.2.2.

3.3.2 Neutron Generator

The neutron generator, NSD-Ng-1e7-DD-Cin, at University of Zurich is used for these measurements. The product is bought from the company NSD-Fusion GmbH, Germany. Detailed technical view of the product can be found in references [54, 55] and a brief explanation about the structure and the neutron production is described here.
NSD generates mono-energetic neutrons with a kinetic energy of 2.45 MeV by deuterium-deuterium fusion [53]:

$$^{2}\mathrm{H} + {}^{2}\mathrm{H} \longrightarrow {}^{3}\mathrm{He} + \mathrm{n}_{2.45\mathrm{MeV}} \tag{18}$$
$$^{2}\mathrm{H} + {}^{2}\mathrm{H} \longrightarrow {}^{3}\mathrm{H} + \mathrm{p}_{3.02\mathrm{MeV}}. \tag{19}$$

Both reactions occur with equal probability. The neutrons are able to escape the vessel practically undisturbed while the protons, ^{3}He, and tritium particles are not able to penetrate the vessel wall. The neutron yield of the generator itself (disregarding the loss due to shielding, aging, performance, etc) is 1.25×10^{7} n/s 4πsr.
In this systems the fusion reaction is accomplished as follows. A reaction chamber is filled with neutral deuterium gas at low pressure. A very high electric field (in the order of 10^{10} V/m) is needed to eventually ionize some deuterium atoms. This enormous electric field is produced by applying high positive voltage (in the range of 100 kV) to a very sharp tip (tip radius in the range of 100 nm). In this strong electric field, the electrostatic potential of an atom is modified and in a certain range

such that there is a possibility for an electron to tunnel into the tip leaving the atom ionized (field ionization). The positively charged atom is then accelerated by the tip's potential away from the tip into a target covered by a deuterium or tritium film [56].
The NSD Neutron Generator uses a gaseous deuterium target. The gas is ionized and the resulting plasma is controlled by inertial-electrostatic-confinement. This increase the lifetime of the generator to 20000 hours without any maintenance according to manufacturer [54].
The neutron generator is placed inside a shielding made of three different layers. The first layer (closest to the generator) is Paraffin. Paraffin, due to its high hydrogen density is a suited for slowing down extremely fast neutrons [57]. The second layer is boron-doped polyethylene (5 % boron). The hydrogen in polyethylene fulfills the same purpose as the paraffin. After the passage through the paraffin, most of the neutrons are slowed down enough for the capture cross section of boron to rise to a very high value and thus be captured. The third layer consists of 35 cm concrete for gamma capturing purposes.
Schematics describing the neutron generation is shown in the Fig. 18. The neutron beam is allowed to pass by a hole of 10 cm diameter in the wall to the room in which the experimental devises (detectors, electronics and etc) are installed. The X-rays are captured by the shielding layers.

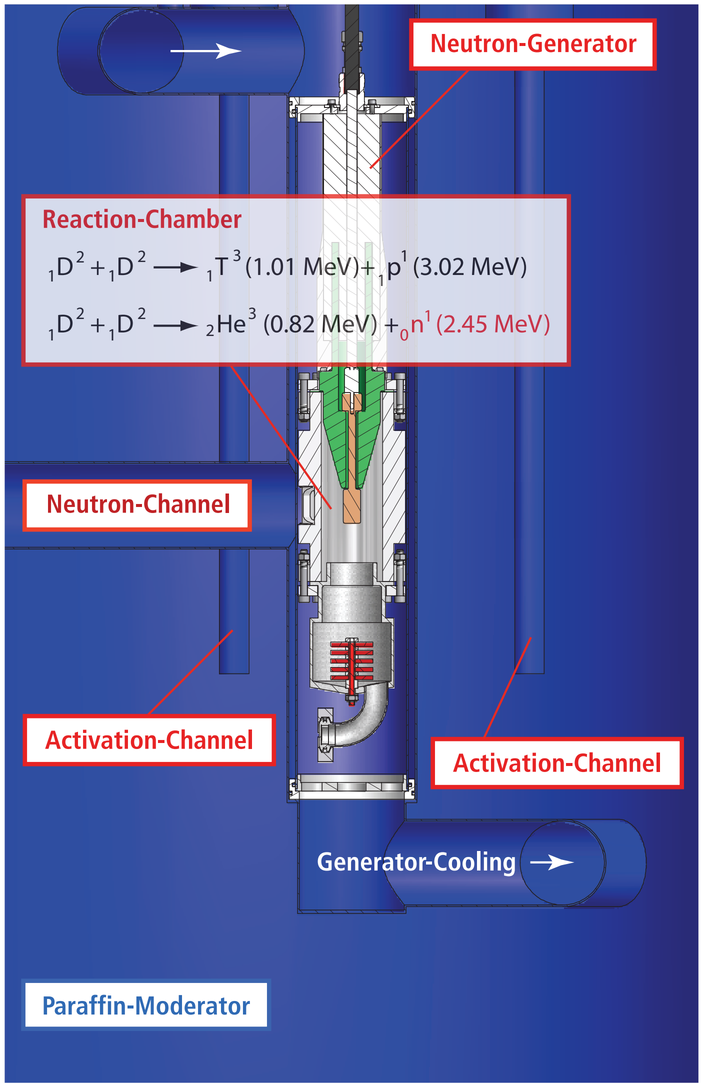

Figure 18: Schematics of NSD neutron generator. Please refer to the text for full explanation. Figure from reference [53].

3.3.3 Signal Readout

The MPD-4 module is used for discrimination purposes and is described in detail in section 2.4.
The time of flight (TOF) module has a “start”and a “stop”input signals and the output is a step signal whose height corresponds to the time between the input signals. Calibration of this module is required to convert the signal height into units of time. This is explained in the results section.
The TOF signal then is fed into a 100 MS/s Analog to Digital Converter and being saved in 200 steps (2 μs) with a delay of 500 ns before the trigger.
A total range of 5 V is used for the signal. The signal is shaped like a step function(see figure 19). The height of this function is proportional to the real time window between “start”and a “stop”triggers. To manipulate the signal the average of the first 40 points in the signal is subtracted from the last 40 and saved as the TOF of the corresponding event (after calibration).

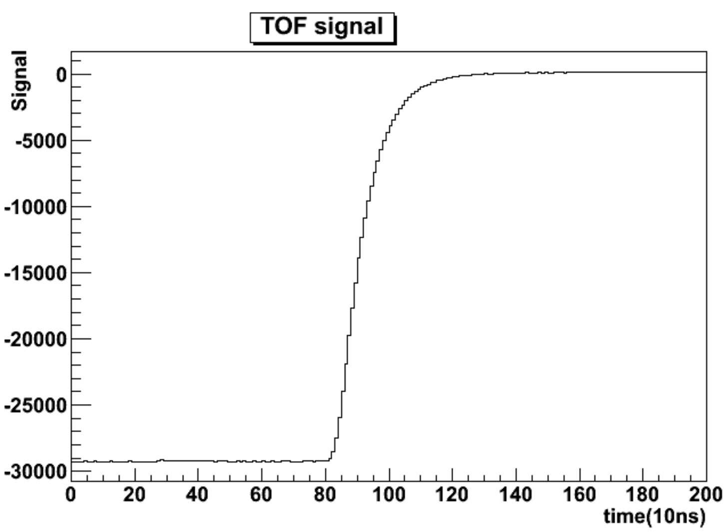

Figure 19: An example of the time of flight waveform. The signal looks like a step function. The height of the signal is proportional to the time of flight.

3.4 Results

3.4.1 Calibration of TOF

As mentioned above, in order to be able to analyze the neutron measurements, a calibration of time of flight signal is required. There are two options to calibrate the time of flight signal.

The first method is to use a automatic pulser device to generate pulses. The output pulses can go into a fan-in fan-out modules to be splitted in two coincidence pulse. One of the outputs can develop a manually defined delay. Then, the direct pulse can be used as "start"and the delayed pulse as the "stop"points of time of flight. The predefined delay can change to a few numbers in the range of expected signal ($\sim 100\,\mathrm{ns}$). Having a few points of measured TOF vs the real delay of the signals in hand, finding a calibration function is straight forward.

The second idea to calibrate the time of flight is to take advantage of interaction 9 of ^{22}Na (see section 2.2.1) radioactive source. In this way, if the source is placed (approximately) in the middle of two EJ301 detectors, a percentage of the final state 511 keV gammas will reach coincidentally both detectors 20. Then it is easy to apply a delay to one of the signals and plot the time of flight which is measured between two signals versus the applied delay (see figure 21a).

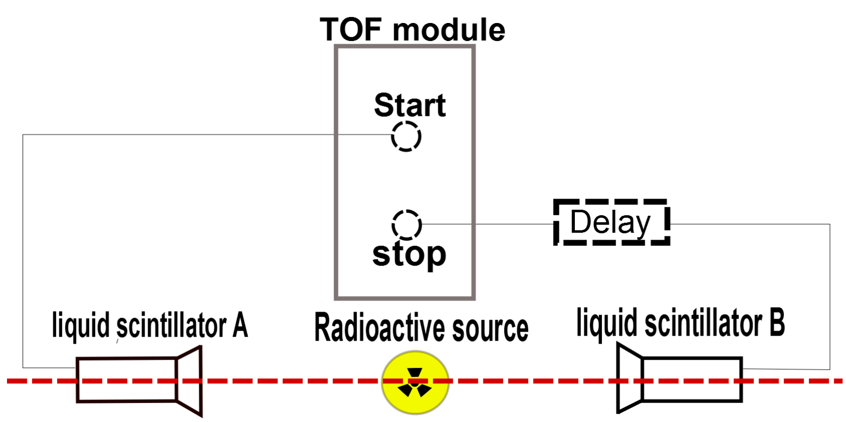

Figure 20: Schematics of the setup prepared for calibration of TOF signal. The 511 keV gammas from the source will reach both detectors simultaneously and produce a coincidence event. The signal from the second detector is then delayed for a certain period to produce manually a time of flight signal.

In our measurements, the second way is preferred since it is more consistent with the final setup with neutrons than using a pulse generator device. Three different delay constants at 30 ns, 60 ns and 100 ns were acquired for the calibration. The TOF spectrum of these events is displayed at Fig. 21a. Numbers on the x-axis correspond to 30 ns, 60 ns and 100 ns of time of flight respectively . The result of these 3 runs and the calibration plot is shown in Fig. **??**.

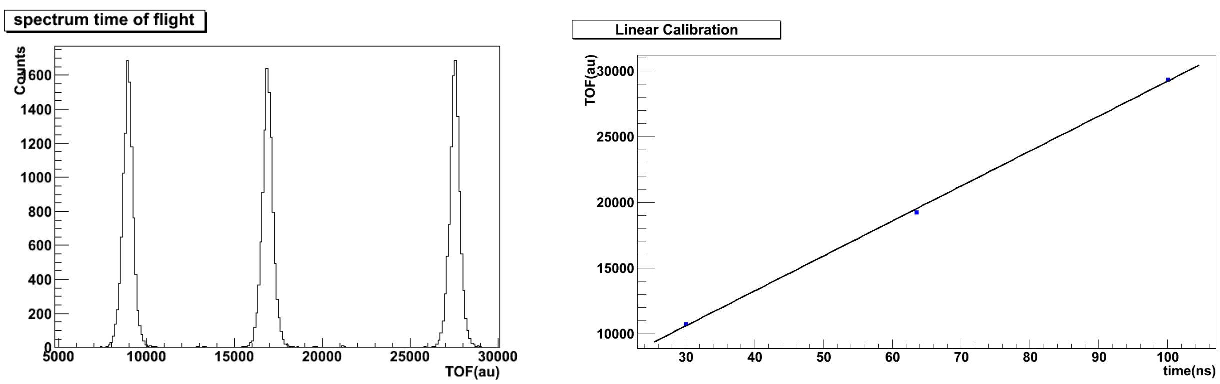

(a) TOF spectrum of 3 calibration runs.

(b) Calibration result.

Figure 21: Calibration results of TOF. Please read the text for description.

3.4.2 Preliminary Runs and Results

In the first run with the neutron generator the distance between the two detectors was fixed at (55 ± 2) cm and the angle at $(20 \pm 2)^\circ$. The errors are due to the uncertainty of the length and angle measurement tools.
The n-dis parameter of MPD-4 device for these measurements is turned up to the maximum value meaning that all events including gammas and neutrons are accepted. The selection is done via TAC vs Ampl plots in software (see Fig. 22). The walk parameter is set to its optimized value. This optimization was performed with ^{241}AmBe source before running the measurement (see section 2.4). It helps the selection of neutrons.

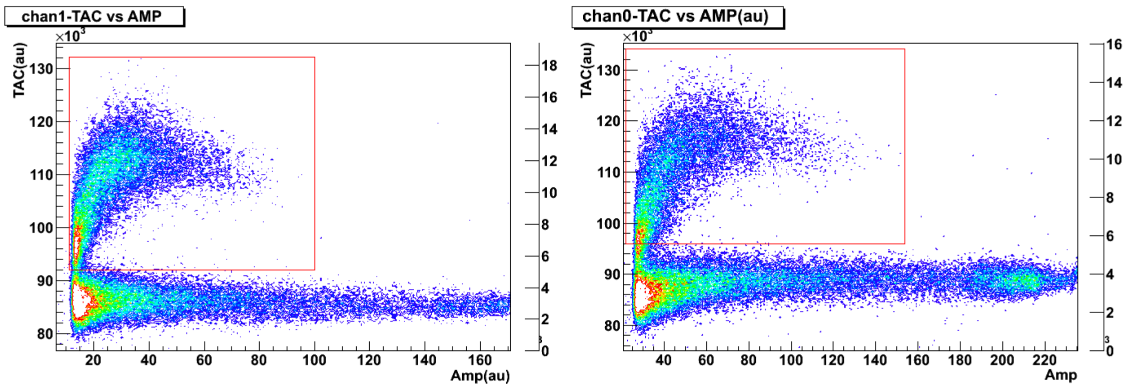

(a) EJ301A

(b) EJ301B

Figure 22: TAC vs Ampl of coincident events. The walk parameter is optimized as the gamma band (lower band) is quite straight. This makes the selection of neutrons (upper band) easier. The events in the boxes are selected as neutrons.

We would expect to see two major peaks in the TOF spectrum. A peak around t=0 should appear due to gamma rays which coincidentally hit the first and second detector. For simplicity we shift all TOF data for -60 ns due to presence of 60 ns offset delay. The second peak should correspond to the neutrons who hit the first scintillator, scatter and hit the second.
The fact that our target material is a composite of carbon and hydrogen atoms, should show up in TOF signal. The reason is, the energy of neutrons scattering with carbons is different from the ones interacting with hydrogen. This is clear looking at equations 14 and 15 (M_N value changes from C (12) to H (1)).
Putting correct values for A into equation 14 and considering $\theta = 20°$ and d= 55 cm one can calculate the energy of neutrons after the first scattering and then the time of flight for distance between two detectors. This calculation gives t= 25 ns for neutrons scattering from carbons while t= 27 ns for scattering with hydrogen targets.
However, the resolution of TOF spectrum is not enough to distinguish points with 2 ns of time difference (see Fig. 23. The first solution to this problem is to increase the distance between two detectors but there are 2 experimental obstacles as follows:

1 : The neutron lab is a small room (~ 2.5 m $\times \sim 2.5$ m) such that distances more than 2.5$-$3 m is not possible.

2 : Increasing the distances between detectors decreases significantly the rate of

detection. When detectors are $\sim 50\,\mathrm{cm}$ away, the rate is about 1 coincidence event every 15 seconds while if we increase the distance the rate would decrease as $\frac{1}{d^2}$ due to solid angle reduction.
This raises two problems by its own. First, there is an internal time-out for the labView program (DAQ) such that it stops working when there is no acquisition for almost 30 seconds (and this cant be edited). Second, with these small rates gathering enough statistics requires long time to wait. A measurement with 50000 events at $d \sim 50\,\mathrm{cm}$ will take around 2 and half days to finish. This would be more than a week for $d \sim 1\,\mathrm{m}$.

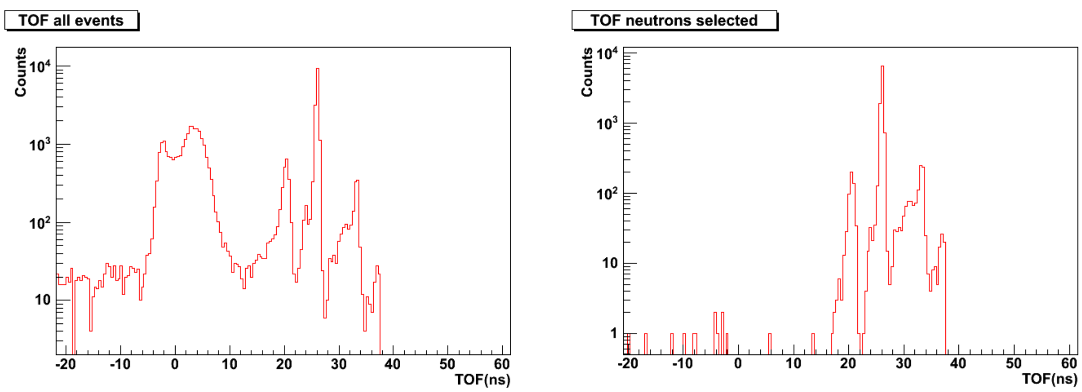

(a) all events (b) neutrons selected

Figure 23: Spectrum of TOF first run. The gamma (photons) represent a time of flight around 0 and are disappeared when the neutrons are selected.

It is important to notice that, so far, we had no explanation about the peaks in Fig. 23 at t=20 ns and t=30 ns. These peaks are one order of magnitude less populated than the main peak at t=26 ns which is due to scattering from carbon and hydrogen atoms. Further measurements are required for more understanding of spectrum (describing unexplained populations) .
The errors which are reducing the resolution of TOF spectrum are mainly caused by the uncertainties in the distances which neutrons have to fly between the two scintillators. First, the distance measurement has its own error. Next, the distance is measured between centers of the scintillators while neutrons might scatter at any point in the scintillators. The active volume of EJ301 has a diameter of 10 cm which means that the side by side distance of detectors is not 55 cm but ≈58 cm. It will take about 0.5 ns for neutrons of these energies to travel 3 cm of distance offset. This

explains why the population of neutrons is $\approx \pm 0.5\,\mathrm{ns}$ wide in TOF spectrum.
It is also interesting to see the Ampl spectrum of the events (only nuclear recoil are selected) both in the first and the second scintillators. This is what is shown in Fig. 24. The X axis is Ampl in arbitrary units (calibration of nuclear recoils in not available).

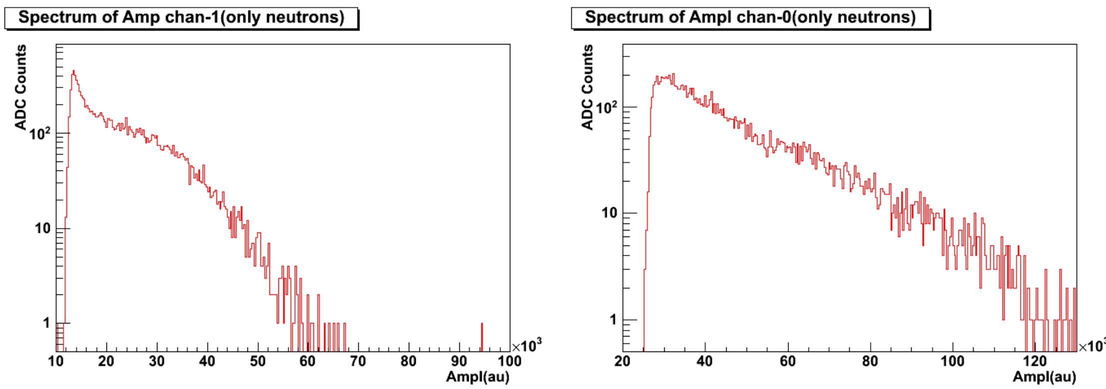

(a) Liquid scintillator A

(b) Liquid scintillator B

Figure 24: Spectrum of Ampl of selected nuclear recoils in a)first both liquid scintillators. Please refer to the text for detailed description.

Ampl corresponds to the energy deposited in the detector by nuclear recoils. This energy depends on the scattering angle as well as other parameters (for example, type of interacting particles). In the second scintillator, it is not known with which angle the particles are scattered. In contrast, in the first scintillator we are only dealing with the particles which scatter with a certain angle i.e. $\theta = 20°$.
This raises the expectation to observe a peak in the Ampl spectrum of the first detector. However, in Fig. 24, we can't see a clear peak i.e. the peak is at the very left and we don't know how much of the real peak is covered. This means that we are probably ignoring (or equivalently not acquiring) most of the nuclear recoils in the low-energy range which is indeed the case of interest of these studies.
The threshold of the acquiring system is set at the minimum and can't be the reason. Thus, the only option is the increase the voltage of the PMT in the EJ301 liquid scintillator so that hopefully it acquires events with lower energies. This will increase or view range of the spectrum shown in Fig. 24 to the left.
A measurement is done when the applied voltage to the PMTs is increased from $-1400\,\mathrm{V}$ up to $-2000\,\mathrm{V}$ thought the result is still to be analyzed.

It is also interesting to look at the plots of component ratio (TAC) versus time of flight of the events in which one expects to see the best discrimination of nuclear and electronic recoils to appear. This is because nuclear recoils defer from electronic recoils both at TOF and TAC values. Figure 25 shows the TAC vs TOF plots of both liquid scintillators A and B.

In this figure, the nuclear recoils are populated at high TOF values and high TAC values and the gammas in contrast represent low TAC and TOF values (actually, time of flight of gammas is very close zero as they travel with the speed of light). The same, still unexplained, populations at t=20 ns and t=30 ns, which were shown in figure 24, are also present here.

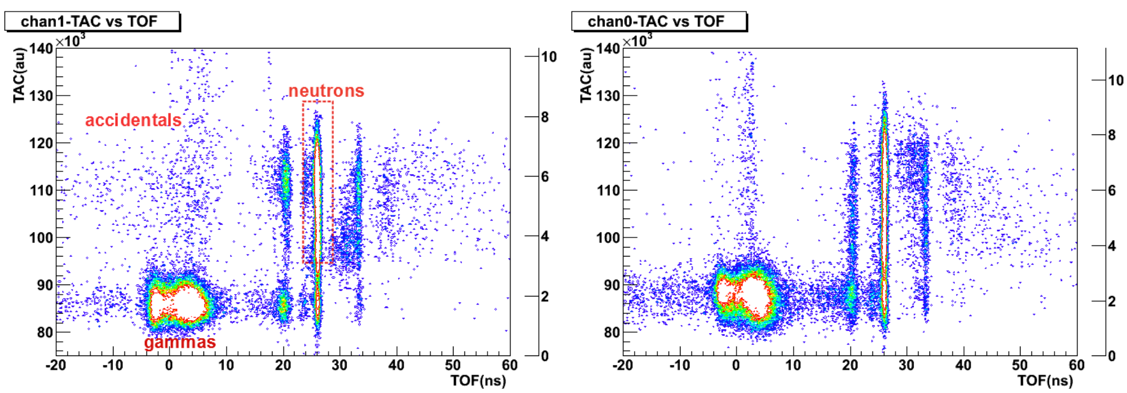

(a) Liquid scintillator A

(b) Liquid scintillator B

Figure 25: Component ratio (TAC) vs time of flight (TOF) of all events recorded in a) liquid scintillator A and b) liquid scintillator B.
The populations corresponding to nuclear recoils, electronic recoils, and accidental events are marked in the figures.

Summary and Outlook

In this work, some experiments are described with their results aiming for preparing required information for a future measurement of the low energy response of liquid xenon.

Chapter 2 discusses the pulse shape discrimination (PSD) studies in organic liquid scintillators. First, it is described how a measurement was set up with a liquid scintillator detector and radioactive sources investigating finding the optimal PSD parameter. Second, to avoid reading the waveform from PMT signal, a pulse shape discrimination module, named MPD-4, was used. Finally, MPD-4 module was characterized meaning to find optimized self-adjustable parameters of the device affecting discrimination performance.

Chapter 3 covers the experimental setup and results of a measurement with a neutron source and two liquid scintillators which aims to characterize the neutron beam. The measurement is done since the same neutron generator will be used in future for studying the low-energy response of liquid xenon to nuclear recoils.

The results of preliminary runs of this experiment shows the lack of resolution to distinguish nuclear recoils in hydrogen atoms from the ones in carbon atoms in the liquid scintillator. This can be solved increasing the distances between two detectors which increases the resolution of time of flight (TOF) of neutrons.

There are unexplained populations of events in the TOF spectrum which requires further studies including running measurements varying the angles between the two detectors and the neutron emitting line.

Additionally, it was concluded to be necessary to increase the voltage powering detectors since the low-energy range of events are not included in the amplitude spectrum with the current setup. At the end, enough information about the energy distribution of neutrons emitted from generator should be provided in future as it is an essential condition for the final measurement of liquid xenon response.

References

[1] Scott Dodelson; Modern Cosmology; Academic Press; (2003)

[2] Katherine Garrett and Gintaras Duda; Dark Matter, a primer; Phys Rev 1006.2483v2; (2011)

[3] Andi Hektor, Martti Raidal,Elmo Tempel1; An evidence for indirect detection of dark matter from galaxy clusters in Fermi-LAT data; arXiv:1207.4466v1 [astro-ph.HE]; (2012)

[4] M. Ribordy; Methods and problems in neutrino observatories; arXiv:1205.4965[astro-ph.HE];(2012)

[5] Peter G. O. Freund; Introduction to Supersymmetry; Cambridge University Press; (1988)

[6] E.Aprile et al; Dark Matter Results from 225 Live Days of XENON100 Data; arXiv:1207.5988[astro-IM]; (2012)

[7] E.Aprile et al; Analysis of the XENON100 Dark Matter Search; arXiv:1207.3458v2[astro-IM]; (2012)

[8] E.Aprile et al; The XENON100 Dark Matter Experiment; arXiv:1107.2155v2 [astro-ph.IM]; (2012)

[9] F. Arneodo et al; First Observation of 140-cm Drift Ionizing Tracks in the ICARUS Liquid-Argon TPC ; Nucl. Instrum. Meth. A449, 147; (2000)

[10] R. Bernabei et al; EPJdirect C 11, 1; (2001).

[11] D. Akimov et al; Measurements of scintillation efficiency and pulse shape for low energy recoils in liquid xenon; D. Phys. Lett. B524, 245; arXiv:0106042[hep-ex]; (2002)

[12] E. Aprile et al; Scintillation Response of Liquid Xenon to Low Energy Nuclear Recoils; Phys. Rev. D72, 072006; arXiv:0503621[astro-ph]; (2005)

[13] Christopher Savage, Graciela Gelmini, Paolo Gondolo, Katherine Freese; Compatibility of DAMA/LIBRA dark matter detection with other searches; JCAP 0904:010, 2009 arXiv:0808.3607v3 [astro-ph]; (2009)

[14] C.E. Aalseth et al; Results from a Search for Light-Mass Dark Matter with a P-type Point Contact Germanium Detector; Phys.Rev.Lett.106:131301,2011 arXiv:1002.4703v2 [astro-ph.CO]; (2011)

[15] Z. Ahmed et al; Current Status CDMS-IICDMS-II; Science 327-1619; (2010)

[16] G. Angloher et al; Results from 730 kg days of the CRESST-II Dark Matter Search; arXiv:1109.0702v1 [astro-ph.CO]; (2011)

[17] E. Aprile et al; Dark Matter Results from 100 Live Days of XENON100 Data; Phys. Rev. Lett. 107, 131302 arXiv:1104.2549[astro-ph]; (2011)

[18] M.W.Goodman and E.Witten; Phys.Rev D31,3059; (1985)

[19] J. Angle, et al; Constraints on inelastic dark matter from XENON10; Phys. Rev. D 80, 115005; (2009)

[20] G.J. Alner et al; ZEPLIN-II: A two phase xenon detector; Astropart. Phys. 28-287; (2007)

[21] E. Aprile, T. Doke; Liquid Xenon Detectors for Particle Physics and Astrophysics; Rev.Mod.Phys.82:2053-2097,2010 arXiv:0910.4956v1 [physics.ins-det]; (2009)

[22] O. Cheshnovsky et al; Chem. Phys. Lett. 15, 475; (1972).

[23] G. Bertone, D.G. Cerdeno, J.I. Collar, B. Odom; WIMP identification through a combined measurement of axial and scalar couplings; Phys.Rev.Lett. 99:151301 ; (2007)

[24] V. N. Lebedenko et al; (ZEPLIN-III) Experiment; Phys. Rev. Lett. 103, 151302 , arXiv:0901.4348; (2009)

[25] A. Minamino; (XMASS)Dark Matter Detection Experiment; Nucl. Instrum. Meth. A623, 448; (2010)

[26] M. Auger et al; Search for Neutrinoless Double-Beta Decay in ^{136}Xe with EXO-200; Phys. Rev. Lett. 109, 032505; (2012)

[27] J. Lindhard and M Scharff; Energy dissipation by ions in the keV region; Phys. Rev. 124, 128- 30; (1961)

[28] A. Hitachi; Properties of liquid xenon scintillation for dark matter searches; Astropart. Phys. 24, 247; (2005)

[29] M. Tanaka et al; LET dependence of scintillation yields in liquid xenon; Nucl. Instrum. Meth. A457. 454; (2001)

[30] A. Manalaysay et al; Spatially uniform calibration of a liquid xenon detector at low energies using ^{83m}Kr; Rev. Sci. Instrum. 81, 073303; (2010)

[31] http://www.home.agilent.com/agilent/home.jspx?cc=CH& lc=ger

[32] E. Aprile et al; New measurement of the relative scintillation efficiency of xenon nuclear recoils below 10 keV; Phys. Rev. C 79, 045807; (2009)

[33] G. F. Knoll; Radiation Detection and Measurement, 3rd ed. Wiley and Sons, Inc; (2000)

[34] http://www.eljentechnology.com

[35] Charles D. Ferguson, Tahseen Kazi, Jdth Brr; Commercial radioactive sources; Monterey Institute of International Studies; (2003)

[36] R.E. Lapp and H.L. Andrews; Nuclear Radiation Physics; Prentice-Hall, Englewood Cliffs, NJ; (1972)

[37] C.Guerrero et al; Analysis of the BC501A neutron detector signals using the true pulse shape; DOI: 10.1016; (2008)

[38] V.P.Chechev,N.K.Kuzmenko; Table of radionucleides; http://www.nucleide.org; (2001)

[39] G.Audi; The NUBASE Evaluation of Nuclear and Decay Properties Nuclear Physics; 729: 3-128. Bibcode 2003NuPhA.729; (2003)

[40] http://www.eljentechnology.com/index.php/joomla-overview/this-is-newest/71-ej-301

[41] http://www.ni.com/labview/.

[42] http://root.cern.ch/drupal/

[43] A. Manzur et al; Scintillation efficiency and ionization yield of liquid xenon for monoenergetic nuclear recoils down to 4 keV; Phys. Rev. C 81, 025808; (2010)

[44] G. Plante et al; New Measurement of the Scintillation Efficiency of Low-Energy Nuclear Recoils in Liquid Xenon; arXiv:1104.2587v1 [nucl-ex]; (2011)

[45] J. B. Birks; Theory and practice of scintillation counting; New York : Macmillan; (1964)

[46] http://www.mesytec.com/

[47] Mesytec GmbH and Co. KG; MPD-4, data sheet V2.11

[48] A. Manalaysay; PhD Thesis; Response of liquid xenon to low-energy ionizing radiation andits use in the XENON10 Dark Matter search; University of florida; (2009)

[49] Teresa Marrodan; PhD Thesis; Measurement of light emission in organic liquid scintillators and studies toward the search for proton decay in the future large-scale detector LENA; University of Munich

[50] V. Chepel et al; Scintillation efficiency of liquid xenon for nuclear recoils with the energy down to 5 keV; DOI:10.1016/j.astropartphys; (2006)

[51] A. Manalaysay; Towards an improved understanding of the relative scintillation efficiency of nuclear recoils in liquid xenon; arXiv:1007.3746v1 [astro-ph.IM]; (2010)

[52] E. Aprile, K. L. Giboni, P. Majewski, K. Ni, and M. Yamashita,R. Hasty, A. Manzur, and D. N. McKinsey; Scintillation response of liquid xenon to low energy nuclear recoils; Phys. Rev. D 72, 072006; (2005)

[53] Adrian Aeschbacher; Bachelor Thesis ;Simulation of a Neutron Generator's Radiation Shield; University of Zurich; (2010)

[54] http://www.nsd-fusion.com.

[55] J. Sved; Technical Information for Support of Operation Permit Applications, Issue 1, Version B; NSD-Fusion Gmb; (2008)

[56] S .Putterman B. Naranjo, J.K. Gimzewski; Observation of nuclear fusion driven by a pyroelectric crystal; Nature, 434:1115-1117; (2005)

[57] Doug Reilly, Norbert Ensslin, Hastings Smith, Sarah Kreiner; Passive Nondestructive Assay of Nuclear Materials; National Technical Information Service; (1991)